

## **CHAPTER IV**

### **RESULTS AND DISCUSSION - Part I**

#### **UH60A Rotor in High Speed Forward Flight**

The hybrid methodology described in the previous chapters has been applied to a number of rotor configurations in forward flight. Sample results are presented in this work for two configurations.

The first case studied in this chapter is that of a UH-60A rotor in high speed forward flight condition. This case was chosen to test the ability of the solver to predict the rotor flows at a high advance ratio, in the presence of transonic flow, 3-D dynamic stall, and elastic deformations. The second case studied is that of an AH-1G helicopter low speed descent flight. This particular flight condition is dominated by BVI phenomena, requiring an accurate modeling of the shed wake strength and geometry. This case is discussed in Chapter V.

#### **4.1 UH-60A Rotor in Forward Flight**

Lorber [110, 111] has documented the flow over a UH-60A rotor for a number of hover and forward flight conditions. This rotor is a four-bladed configuration, typical of that found on a current generation army helicopter. It has a complex blade form that tends to complicate numerical analysis, especially in forward flight. The features of the blade include nonlinear twist distribution, several unsymmetrical airfoil sections, and tip sweep. Substantial torsional deformation of the model was observed in the experiment and has been documented. This elastic deformation should be included in any forward flight analysis.

The flow condition simulated in this calculation is for a high speed forward flight with an advance ratio of 0.3 and a tip mach number of 0.628. Figure 4.1 shows a schematic representation of the model UH-60A rotor planform.

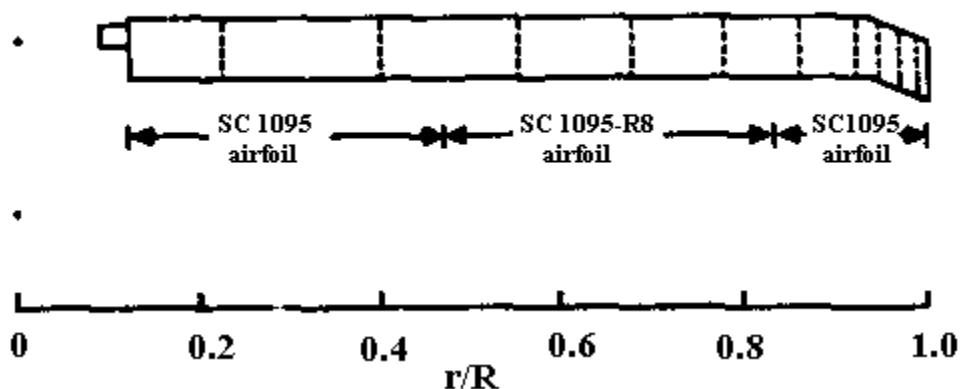


Figure 4.1: Planform of the UH-60A Model Rotor

The blade has an aspect ratio of 15.3, and a maximum twist of 13 degrees. The structural twist distribution reproduced from Ref. [110] is shown in Figure 4.2. The blade

has a rearward sweep of 20 degrees starting from the radius of 93%. The blade is made up of two airfoil sections SC1095 and SC1095R8.

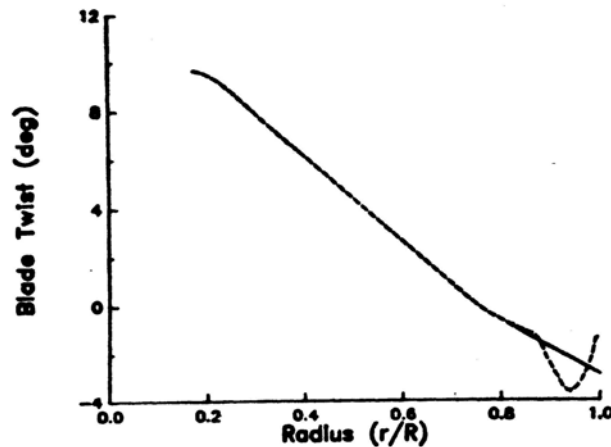


Fig.4.2: Geometric Twist Distribution for the UH-60A Rotor

In the experiment, the blades were trimmed to eliminate the one-per-rev flapping. The rotor blade sectional twist including elastic deformation is available at several radial locations at different azimuthal locations. Figure 4.3 is taken from Lorber's data [111] and includes the collective and cyclic pitch, the built-in structural twist distribution, and the torsional deformations around the azimuth. The collective pitch was chosen, following a trim analysis to match the computed thrust coefficients with measured data, as 11.5 degrees. The blade pitch variation at 75%R, neglecting elastic deformation which modify the sectional pitch angles, may be approximated as follows:

$$\theta = 11.5^\circ + 1.84^\circ \cos \psi - 7.5^\circ \sin \psi \quad (4.1)$$

As can be seen in figure 4.3, the measured pitch variation is not purely sinusoidal because of elastic deformations. The differences between the measured angles and the below cyclic pitch distribution were bilinearly interpolated radially and temporally, and incorporated in the analysis through transpiration boundary conditions, as discussed in Chapter III.

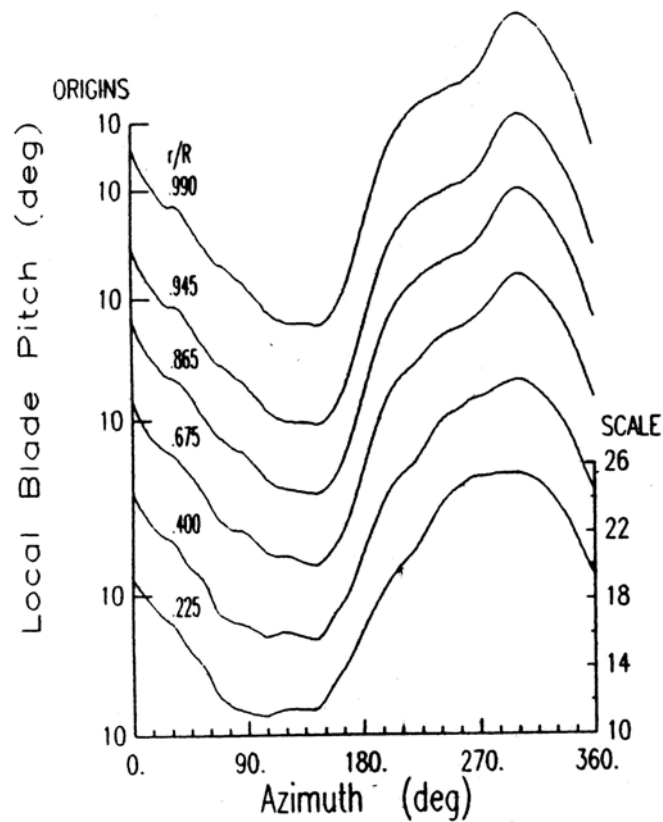


Fig.4.3: Measured Pitch Angle Variations with Azimuth at Several Radial Locations,

Level flight at  $\mu=0.3$

Several calculations for this rotor configuration have been presented in literature. Ramachandran and Caradonna [21] performed some computations using the vorticity embedding method with full potential equation and the Lagrangean convection of the rotor wake. A total number of 380,000 grid points were used in their calculation. The initial bound circulation and a rigid wake geometry from a comprehensive analysis were used to start the calculation. They reported that a periodic solution was obtained in three blade revolutions. More recently, Bangalore, Moulton and Caradonna [85] studied the UH-60A rotor configuration using an overset/hybrid method that combines a viscous flow solver near the blade surface with a vorticity embedding potential method in the far-field. For the forward flight case in their study, the results presented were from two solutions. The first is a hybrid calculation where the far-field wake effects are supplied by the comprehensive code CAMRAD/JA. The second is a full-potential overset solution that models the wake using the vorticity embedding method. Comparisons between their method, and the present method are included in this study, as part of the code validation.

## **4.2 Computational Grid for the UH-60A Rotor**

An H-O multi-block computational grid is used in this calculation. A typical grid with 320,000 points per blade was used to resolve the boundary layer on the blade surface, and adequately resolve the computational domain. Approximately 38% of the computational nodes fall in the Navier-Stokes zone. There are two blocks, one above the blade, and the other below the blade. The grid system spans 90 degrees in the azimuthal

direction, and consists of 90 points in the azimuthal direction, 44 points in the spanwise direction, and 80 points in the normal direction (with 40 points in each block). The far-field boundary in the radial direction extends one rotor radius beyond the tip. The rotor boundaries in the normal direction were approximately 0.8 radii away from the blade. Such a small computational domain was found adequate in the present study, since the Biot-Savart law provides the velocity field at these boundaries in an accurate and efficient manner. In a conventional analysis, these boundaries would have to be placed much farther away in order to reduce the errors associated with the boundary condition treatment.

The first point normal to the blade surface was 0.0005 chords away from the surface. This value was chosen as a compromise between the resolution of the viscous flow region, and the largest time step which may be taken without instabilities.

At the each radial location, H-grids are generated on and beyond the rotor blade. The radial distribution near the tip may be easily controlled and may be given as a table input. The three-dimensional, multi-block grids are constructed from an assembly of these two-dimensional H-grids. The H-O grids are of H-type in the streamwise and normal directions, and O-type in the azimuthal direction. A typical multi-block H-O grid system around a single blade is shown in Figure 4.4. The H type grids in a particular radial cross section are shown in Figure 4.5. The top view of the O type grid is shown in Figure 4.5. The clustering of the grid points around the blade is also illustrated in these figures. The aspect ratio of the grid cells and the orthogonality of grid lines strongly influence the accuracy and the numerical stability of the solution process.

In forward flight, each rotor blade undergoes different flow conditions, and there is no blade to blade periodicity, as in hover. As stated earlier, the hybrid solver has the advantage of just resolving one blade and does not apply the periodicity boundary conditions. There is no need to restrict the far-field (upstream and downstream) boundaries in the azimuthal direction to a quarter of the rotor disk for a four-bladed rotor. The velocity boundary conditions at these locations are directly computed using Biot-Savart law. The pressure and density at these boundaries are computed from isentropic potential flow, as part of the potential flow solution process, as discussed in Chapters II and III.

### **4.3 Computational Time Requirements for the Hybrid Method**

In forward flight, the hybrid method is about six times faster than a comparable full Navier-Stokes solver for the following reasons:

1. CPU time is reduced by performing hybrid analysis for a single blade. The influences of the other blades are modeled as a collection of bound and tip vortices. This is very useful in forward flight simulations because it allows complex blade pitching and flapping motion to be modeled rapidly without need for inter-blade grid continuity. In many conventional Navier-Stokes analyses, all the blades must be resolved because the flow is no longer symmetric from blade to blade. Resolving all blades leads to the complex

matching and patching of the grids around multiple moving, deforming blades.

2. Because of the Lagrangean tip vortex model in the hybrid method, the number of nodes in the computational grid can be greatly reduced. There is no need for a fine grid that captures several revolutions of the tip vortex.
3. In the hybrid analysis, more than half of the total grid points are in full potential zone. The full potential flow solver is much faster than the Navier-Stokes solver.
4. In a typical Navier-Stokes analysis, the calculations start with a uniform flow field as a starting solution. Several blade revolutions are needed to adequately establish the wake structure and the inflow. The present hybrid method starts with a good estimate of the inflow (Glauert's theory or Biot-Savart Law) and tip vortex structure (rigid helical wake). Calculations converge quickly, usually in 2 or 3 revolutions.

Table 4.1 shows the CPU time usage of the hybrid method compared with that of the conventional Navier-Stokes method. The CPU times reported are based on calculations on a Silicon Graphics O2 system with a R5000 processor. The grid size for the conventional Navier-Stokes method in the table is the same as that for the hybrid method. This table therefore does not take into account the fact that more grid points are usually needed in conventional Navier-Stokes methods to capture the tip vortex strength without much diffusion. Note also that this table takes into account the CPU time needed to update the induced velocity once every 5 degrees of azimuth. This step is costly and requires approximately 140 seconds of CPU time. Fortunately, this update needs to be

done only once every  $5^\circ$  azimuth, or every 100 time steps. The updating interval of every  $5^\circ$  was appropriate for capturing the blade vortex interaction and was discussed in Chapter V. This was also justified by other studies[6, 10, 20, 21].

	Hybrid Method (grid size: 310,000; 1 blade)	Conventional NS Method (grid size: 310,000 per blade; 4 blades)
Time/step (second)	NS (39% total grids): 8 sec.	80 sec.
	FPE (61% total grids): 3 sec.	
	Wake update (every 100 steps): 1.4 sec. per step	
	Total: 12.4 sec.	
Total No. of time step (2 revolutions)	14400	14400
Total CPU time	49.6 hours	320 hours

Table 4.1: Comparison of CPU Time for the Navier-Stokes and Hybrid Methods

#### 4.4 Results and Discussion

The calculations documented in this section were computed using the prescribed wake model, with the spacing between successive vortex rings determined using Glauert's theory. The induced velocities  $\vec{V}_w$  in the outer region and the far-field boundaries were computed using Biot-Savart's law, unless otherwise specified. At the

high advance ratios considered here ( $\mu=0.3$ ), a rigid wake representation is considered to be more than adequate [6].

Figures 4.6-4.15 show the computed and measured surface pressure coefficients at a number of radial sections over a complete revolution. The surface pressure values are non-dimensionlized with respect to the local dynamic pressure. The solid lines represent the upper surface pressure and the dashed lines represent the lower surface pressure calculated by the hybrid method. The experimental data are shown as separate symbols.

Figures 4.6-4.12 show the results for the first quadrant and second quadrant. The surface pressure distribution at 67.5%, 77.5%, 86.5% and 94.5% span stations are shown. At the  $0^{\circ}$  and  $30^{\circ}$  azimuth, the pressures both inboard and outboard are well predicted, and the suction peaks are also captured well. Between  $90^{\circ}$  and  $160^{\circ}$  azimuth, the experimental data shows negative loads in the tip region, because the blade is highly twisted and is pitched down. The computed results in outboard section 94.5% are seen to correctly capture the negative lift. Between  $\Psi=90^{\circ}$  and  $\Psi=120^{\circ}$ , regions of supersonic flow are also observed in tip the region over the first 20% of the chord near the leading edge on the lower surface, both in the experiment and the computations. Figure 4.16 shows the Mach number contours at 96% radial location at  $\Psi=90^{\circ}$ . The supersonic region is clearly visible on the lower surface, and is attributable to a combination of high relative Mach numbers and negative blade angle-of-attack. It is also seen that the pressure field varies smoothly between the inner viscous flow region and the outer potential flow region, with no evidence of any false reflections at the interface.

On the retreating side of the rotor, the flow field is more complex, due to the presence of 3-D separated flow, and dynamic stall phenomena. The pressure distribution at the 67.5% and 94.5% span locations are shown in Figure 4.13-4.15. The present simulations do a good job of modeling the pressure field at the outboard location of 94.5%, but tend to miss the suction peak at the inboard location of 67.5%. Previous studies by Bangalore [88] and Berezin [91] show a similar trend in that the suction peak at the inboard locations are consistently underpredicted.

The fact that the discrepancies occur only over the first 20% of the chord indicates that these are not attributable to angle of attack effects (caused by elastic deformation), which would change the pressure field everywhere, not just the leading edge region. These discrepancies are also not attributable to the grid spacing in the leading edge region because good agreement is observed at other locations (94.5%R) where a comparable grid spacing exists. These discrepancies may, however, be attributable to a lack of convergence of the flow field at the inboard stations, and the inflow model. A study was done to examine the source of the discrepancy at inboard locations and is discussed later.

The sectional normal force coefficients are shown in Fig.4.17 at three radial locations. The experimental data is taken from Lorber's study [111]. In order to isolate the effects of the elastic deformations, both a rigid blade simulation and simulations that account for the torsional deformations are shown. It is seen that the inclusion of the elastic effects dramatically improves the correlation with measurements. It is seen that the sectional normal force is a strong function of the blade position, and closely follows the blade pitch distribution along the azimuth. The normal force at the inboard location

$r/R=67.5\%$  is underpredicted in the second and third quadrants. This is associated with the under-prediction of the leading edge suction, and the causes discussed in the previous paragraph.

At the outboard region, the normal force coefficients at 78% and 92% compare fairly well with the experimental data. The experimental data show a large increase in the normal force coefficients with  $\Psi$  on the advancing side and the magnitude of the negative lift increases with the radial location. The drop was not properly captured in the rigid rotor simulations. With the inclusion of the elastic deformation, the negative lift is captured well, and the fact that the negative lift increases with radial distance also can be seen. This conforms to the suggestion by Ramachandran and Caradonna [21] that the negative lift is related to rotor deformation, and that the model rotor is experiencing a sizable nose down twist.

The results computed by Bangalore, Moulton and Caradonna [85] are compared with the hybrid method in Figure 4.18. They concluded that the difference on the retreating side in their results was due to an occurrence of dynamic stall on the inboard portions that their potential flow model was not capable of predicting. The present viscous method is able to capture most of the variations attributable to mild dynamic stall and may be considered an improvement over inviscid analyses.

In an effort to improve the correlation with experimental data, especially in the inboard region on the advancing side, the grid was refined along the spanwise direction (55 nodes) with more grid points in the inboard region. Figure 4.20 shows that the computed loads are nearly insensitive to the grid density, at least for these two grids. At the particular azimuthal position  $\Psi=90^0$ , a quasi-steady solution was computed to trace

the cause of discrepancies at the inboard locations. The hybrid code was modified to perform quasi-steady simulations, for a specified azimuth location of the blade, and flight conditions ( $C_T$ , tip Mach number, advance ratio). Two different inflow models were used in the calculations to define the wake model and for computing the rotational flow velocity  $\vec{V}_w$ . In the first simulation,  $\vec{V}_w$  was set to be constant everywhere in the flow field, at a value given by Glauert's theory. In the second simulation, a rigid wake model was assumed with vortex ring spacing given by Glauert's theory, with  $\vec{V}_w$  computed using the Biot-Savart's law.

Figure 4.19 shows the convergence history of the sectional normal force coefficients at different radial locations using the two wake models. Note that this is a quasi-steady simulation, and the solution converges to a "steady" state value. Such a quasi-steady simulation is economical and permits a systematic testing of inflow models. The calculations were run for approximately 20 chords of blade travel at the 75% radius. The steady values of the sectional normal force coefficient at three different radial locations are plotted in the Figure 4.20, along with the previously shown unsteady solutions. The quasi-steady results computed with the uniform inflow model are closest to the experimental data. The quasi-steady result with non-uniform inflow was quite close to the previously computed unsteady solution. Based on these simulations, one can conclude that the discrepancies are attributable to the inflow model, and that the Biot-Savart law based inflow model may be underestimating the induced velocity field, and the associated changes to the blade angle attack effects. Further studies aimed at improved estimates of  $\vec{V}_w$  are warranted.

The sectional normal force coefficients in Figure 4.20 show poor correlation over some of the azimuth range. The hybrid solution is started from uniform freestream flow, which is not the true flowfield about the blade. Smith et al [75] showed that the convergence and accuracy of Euler/Navier-Stokes aeroelastic solutions of rotors in hover are directly controlled by the starting flowfield. She recommended a partially- or fully-converged quasi-steady solution as the starting flowfield so that the numerical simulation is only required to capture the unsteady aerodynamic and aeroelastic effects about the mean quasi-steady flowfield. This approach was implemented into the present study, and the results are also shown in Figure 4.20. It is readily observed that on the first iteration the loads at the  $90^{\circ}$  azimuth location are captured much more accurately than the converged hybrid solution after 2 revolutions. However, stability problems were encountered using the quasi-steady results, which indicates that further stability analyses concerning the wake and aeroelastic updating method need to be investigated.